

1 **Effects of  $\alpha$ -tubulin acetylation on microtubule structure and stability**

2 Lisa Eshun-Wilson<sup>1</sup>, Rui Zhang<sup>2,11</sup>, Didier Portran<sup>3,9</sup>, Maxence Nachury<sup>3</sup>, Dan Toso<sup>4</sup>,  
3 Thomas Lohr<sup>5</sup>, Michele Vendruscolo<sup>5</sup>, Massimiliano Bonomi<sup>5,10</sup>, James S. Fraser<sup>6,7\*</sup> Eva  
4 Nogales<sup>1,4,7,8\*</sup>

5 <sup>1</sup>Department of Molecular and Cellular Biology, University of California, Berkeley, CA  
6 94720

7 <sup>2</sup>Department of Biochemistry and Molecular Biophysics, University of Washington School  
8 of Medicine, St. Louis, MO 63130

9 <sup>3</sup>Department of Ophthalmology, University of California, San Francisco, CA 94158

10 <sup>4</sup>California Institute for Quantitative Biology (QB3), University of California, Berkeley, CA  
11 94720

12 <sup>5</sup>Department of Chemistry, University of Cambridge, CB2 1EW, UK

13  
14 <sup>6</sup>Department of Bioengineering and Therapeutic Sciences, University of California, San  
15 Francisco, CA 94158

16 <sup>7</sup>Molecular Biophysics and Integrated Bioimaging Division, Lawrence Berkeley National  
17 Laboratory, Berkeley, CA 94720

18 <sup>8</sup>Howard Hughes Medical Institute, University of California, Berkeley, CA 94720

19 <sup>9</sup>Centre de Biologie Cellulaire de Montpellier (CRBM), CNRS, Univ. Montpellier,  
20 UMR5237, Montpellier 34090, France

21 <sup>10</sup>Current address: Structural Bioinformatics Unit, Institut Pasteur, CNRS UMR 3528,  
22 75015 Paris, France

23 <sup>11</sup>Current address: Department of Biochemistry and Molecular Biophysics, Washington  
24 University in St. Louis, St. Louis, MO, 63110

25 \*Co-corresponding author: [jfraser@fraserlab.com](mailto:jfraser@fraserlab.com)

26 \*Co-corresponding author: [enogales@lbl.gov](mailto:enogales@lbl.gov)

27

## 28 **ABSTRACT**

29 Acetylation of K40 in  $\alpha$ -tubulin is the sole post-translational modification to mark the  
30 luminal surface of microtubules. It is still controversial whether its relationship with  
31 microtubule stabilization is correlative or causative. We have obtained high-resolution  
32 cryo-electron microscopy reconstructions of pure samples of  $\alpha$ TAT1-acetylated and  
33 SIRT2-deacetylated microtubules to visualize the structural consequences of this  
34 modification and reveal its potential for influencing the larger assembly properties of  
35 microtubules. We modeled the conformational ensembles of the unmodified and  
36 acetylated states by using the experimental cryo-EM density as the structural restraint in  
37 molecular dynamics simulations. We found that acetylation alters the conformational  
38 landscape of the flexible loop that contains  $\alpha$ K40. Modification of  $\alpha$ K40 reduces the  
39 disorder of the loop and restricts the states that it samples. We propose that the change  
40 in conformational sampling that we describe, at a location very close to the lateral contacts  
41 site, is likely to affect microtubule stability and function.

42

## 43 **ABBREVIATIONS**

44 MT, microtubule; PF, protofilament; PTM, post-translational modification; MAP,  
45 microtubule-associated protein;  $\alpha$ TAT1, acetyltransferase TAT1 for  $\alpha$ -tubulin; SIRT2  
46 deacetylase SIRT2.

47

## 48 INTRODUCTION

49 Microtubules (MTs) are essential cytoskeletal polymers important for cell shape  
50 and motility and critical for cell division. They are built of  $\alpha\beta$ -tubulin heterodimers that  
51 assemble head-to-tail into ~13 polar protofilaments (PFs), which associate laterally to  
52 form a hollow tube<sup>1</sup>. Lateral contacts involve key residues in the so-called M-loop  
53 (between S7 and H9) in one tubulin monomer and the H2-H3 loop and  $\beta$ -hairpin structure  
54 in the H1'-S2 loop of the other tubulin subunit across the lateral interface. These lateral  
55 contacts are homotypic ( $\alpha$ - $\alpha$  and  $\beta$ - $\beta$  contacts), except at the MT “seam”, where the  
56 contacts are heterotypic ( $\alpha$ - $\beta$  and  $\beta$ - $\alpha$  contacts)<sup>2</sup>. MTs undergo dynamic instability, the  
57 stochastic switching between growing and shrinking states<sup>3,4</sup>. These dynamics are highly  
58 regulated *in vivo* by multiple mechanisms that affect tubulin and its interaction with a large  
59 number of regulatory factors.

60 One mechanism that cells can use to manipulate MT structure and function  
61 involves the post-translational modification of tubulin subunits. Through the spatial-  
62 temporal regulation of proteins by the covalent attachment of additional chemical groups,  
63 proteolytic cleavage or intein splicing, post-translational modifications (PTMs) can play  
64 important roles in controlling the stability and function of MTs<sup>5</sup>. Most of tubulin PTMs alter  
65 residues within the highly flexible C-terminal tail of tubulin that extends from the surface  
66 of the MT and contributes to the binding of microtubule-associated proteins (MAPs)<sup>6,7</sup>.  
67 These PTMs include detyrosination,  $\Delta 2$ -tubulin generation, polyglutamylation, and  
68 polyglycylation<sup>8</sup>. However, acetylation of  $\alpha$ -tubulin on the K40 stands out as the only  
69 tubulin PTM that localizes to the inside of the MT, within a loop of residues P37 to D47,

70 often referred to as the  $\alpha$ K40 loop. This modification is carried out by  $\alpha$ -tubulin  
71 acetyltransferase  $\alpha$ TAT1 and removed by the NAD<sup>+</sup>-dependent deacetylase SIRT2 and  
72 by HDAC6<sup>6,9</sup>. How the enzymes interact with the  $\alpha$ K40 luminal loop, and whether this  
73 “hidden PTM” has a causative or correlative effect on MT properties remain elusive.

74         Shortly after its discovery over 30 years ago<sup>10</sup>, acetylation of  $\alpha$ K40 was found to  
75 mark stable, long-lived ( $t_{1/2}$  >2 hours) MT subpopulations, including the axonemes of cilia  
76 and flagella or the marginal bands of platelets<sup>6,9</sup>, and to protect MTs from mild treatments  
77 with depolymerizing drugs, such as colchicine<sup>11</sup> and nocodazole<sup>12</sup>. Multiple studies have  
78 shown that reduced levels of  $\alpha$ K40 acetylation cause axonal transport defects associated  
79 with Huntington’s disease, Charcot-Marie-Tooth disease, amyotrophic lateral sclerosis,  
80 and Parkinson’s disease<sup>13–16</sup>. These defects can be reversed by restoring  $\alpha$ K40  
81 acetylation levels<sup>17</sup>. On the other hand, elevated levels of  $\alpha$ K40 acetylation promote cell-  
82 cell aggregation, migration and tumor reattachment in multiple aggressive, metastatic  
83 breast cancer cell lines<sup>18,19</sup>.

84         Whether acetylated MTs are stable because they are acetylated or whether stable  
85 structures are better at acquiring this modification remains a point of contention. For  
86 example, a previous study showed that acetylation did not affect tubulin polymerization  
87 kinetics *in vitro*<sup>20</sup>. However, this study was confounded by two factors: (i) microtubules  
88 acetylated by flagellar extract were compared to native brain tubulin, which is  
89 approximately 30% acetylated and (ii) only a single round of  
90 polymerization/depolymerization was performed after *in vitro* acetylation, which is  
91 insufficient to remove  $\alpha$ TAT1 or other MAPs. Thus, the results of this study may be limited

92 by the purity and preparation of the sample. Our previous structural work also found no  
93 significant differences between 30% acetylated and 90% deacetylated MTs at a resolution  
94 of  $\sim 9$  Å, particularly at the modification site, the  $\alpha$ K40 residue within the  $\alpha$ K40 loop, which  
95 was invisible in both cases due to the intrinsic disorder and/or to the remaining  
96 heterogeneity of the loop (i.e. that study may have been limited by the low purity of the  
97 samples)<sup>9</sup>. More recent *in vitro* studies, using pure samples of 96% acetylated and 99%  
98 deacetylated MTs, argue that  $\alpha$ K40 acetylation induces a structural change that improves  
99 the flexibility and resilience of MTs<sup>21,22</sup>. These studies find that acetylated MTs maintain  
100 their flexural rigidity, or persistence length, after repeated rounds of mechanical stress,  
101 while deacetylated MTs show a 50% decrease in rigidity and are 26% more likely to suffer  
102 from complete breakage events<sup>21,22</sup>.

103         Since the  $\alpha$ K40 residue is less than 15 Å away from the lateral interface between  
104 protofilaments, a possible model for the molecular mechanism of acetylation is that it  
105 alters inter-protofilament interactions by promoting a conformation of the  $\alpha$ K40 loop that  
106 confers flexural rigidity, thus increases its resistance to mechanical stress—a  
107 phenomenon called protofilament sliding<sup>21,22</sup>. Molecular dynamics simulations have  
108 suggested a model where  $\alpha$ K40 forms a stabilizing salt bridge with  $\alpha$ E55 within the core  
109 of the  $\alpha$ -tubulin monomer that in turn stabilizes  $\alpha$ H283 within the M-loop of its neighboring  
110  $\alpha$ -tubulin monomer<sup>23</sup>. Another study proposed that  $\alpha$ K40 acetylation may specify 15-PF  
111 MTs, which are known to be 35% stiffer than 13PF MTs and more effective at forming  
112 microtubule bundles<sup>24</sup>.

113           Given the uncertainties remaining concerning the effect of  $\alpha$ K40 acetylation on  
114 MTs, we decided to characterize the conformational properties of the  $\alpha$ K40 loop in the  
115 acetylated and deacetylated MTs that could have an effect on MT structure and  
116 properties. To that end, we produced near atomic-resolution cryo-EM maps of 96%  
117 acetylated ( $\text{Ac}^{96}$ ) and 99% deacetylated ( $\text{Ac}^0$ ) MTs. By improving sample purity, we were  
118 able to visualize more density for the  $\alpha$ K40 loop in the acetylated state. Using new  
119 molecular dynamics methods, we found that acetylation shifts the conformational  
120 landscape of the  $\alpha$ K40 loop by restricting the range of motion of the loop. In contrast, in  
121 the  $\text{Ac}^0$  state, the  $\alpha$ K40 loop extends deeper into the lumen of the MT, and samples a  
122 greater number of conformations. These motions are likely to increase the accessibility  
123 of the loop to  $\alpha$ TAT1, in agreement with the hypothesis that  $\alpha$ TAT1 acts by accessing the  
124 MT lumen<sup>25</sup>, and likely influence lateral contacts, in agreement with the causative effect  
125 of acetylation on the mechanical properties of microtubules<sup>21</sup>.

126

## 127 **RESULTS AND DISCUSSION**

### 128 ***High-resolution cryoEM reconstructions of pure acetylated ( $\text{Ac}^{96}$ ) and deacetylated*** 129 ***( $\text{Ac}^0$ ) MTs***

130           Using recent biochemical schemes designed to enrich for specific acetylation  
131 states<sup>21</sup>, we generated  $\text{Ac}^{96}$  and  $\text{Ac}^0$  MTs for use in our cryo-EM studies. We prepared  
132 cryo-EM samples as previously described<sup>2,26</sup> of  $\text{Ac}^{96}$  and  $\text{Ac}^0$  MTs in the presence of end-  
133 binding protein 3 (EB3). EB3 served as a fiducial marker of the dimer that facilitated  
134 alignment of MT segments during image processing<sup>27</sup>. Table S1 summarizes the data

135 collection, refinement, and validation statistics for each high-resolution map we visualized  
136 (see also Supplemental Figures 1 and 2). Using the symmetrized MT reconstruction,  
137 which takes advantage of the pseudo-helical symmetry present in the MT, we extracted  
138 a 4x3 array of dimers for further B-factor sharpening, refinement<sup>28</sup>, and model-building  
139 (Figure 1a). This array includes all possible lateral and longitudinal non-seam contacts  
140 for the central dimer, which was later extracted for model building and map analysis  
141 (Figure 1b,1c).

142         The  $\alpha$ K40 loop has been poorly resolved in previous EM reconstructions, and  
143 existing models contain a gap between residues Pro37 and Asp48 (Supplemental Figure  
144 3a)<sup>25</sup>. While the loop has been resolved in a number of X-ray crystallographic structures,  
145 the conformations stabilized in the crystal lattice are likely artifacts due to the presence  
146 of calcium and/or crystal contacts (Supplemental Figure 3b). For our symmetrized maps,  
147 we were able to build residues S38-D39 and G44-D47 into the Ac<sup>96</sup> state and S38 and  
148 D46-D47 into the Ac<sup>0</sup> state (Figure 1d, 1e). Qualitatively, the maps suggest that the  $\alpha$ K40  
149 loop is slightly more ordered in the Ac<sup>96</sup> state, with the protrusion of density following  
150 Pro37 extending away from or toward Asp48 in the Ac<sup>96</sup> or Ac<sup>0</sup> states, respectively.  
151 However, it is likely that multiple conformations of the loop, perhaps as a function of each  
152 loop's individual position around a helical turn, are averaged together and result in the  
153 low signal-to-noise levels we observe in the map.

154 ***Conformational differences across MT states are confirmed by non-symmetrized***  
155 ***reconstructions***

156 We considered the possibility that the symmetrizing procedure used to improve  
157 signal and resolution in our image analysis was averaging different  $\alpha$ K40 loop  
158 conformation within different PFs and thus interfering with our interpretation of the loop  
159 structure in the two states. To test the hypothesis, we analyzed the non-symmetrized  
160 maps calculated with C1 symmetry for the  $Ac^{96}$  and  $Ac^0$  states. We extracted a full turn of  
161 13 adjacent dimers. This full-turn map revealed additional density extending out further  
162 along the loop in the  $Ac^{96}$  state when compared to the symmetrized maps filtered to the  
163 same resolution (4 Å) (Figure 2). Furthermore, the density for the loop observed at the  
164 seam was distinct from that at the non-seam contacts. To maximize the interpretability of  
165 the subunits making non-seam contacts, we used non-crystallographic symmetry (NCS)  
166 averaging as an alternative method to increase the signal-to-noise levels in the maps.  
167 This procedure improved the density for non-Glycine backbone atoms in the  $\alpha$ K40 loop  
168 in the  $Ac^{96}$  state, allowing us to trace an initial C $\alpha$  backbone for this region, while in the  
169  $Ac^0$  state the loop remained unmodelable (Figure 2c, 2d). This interpretation agrees with  
170 the qualitative difference in the density, which indicate less disorder for the  $Ac^{96}$  state than  
171  $Ac^0$  state, of the traditionally symmetrized and C1 maps.

172 This NCS averaging method had multiple advantages over the traditional  
173 averaging technique for pseudo-helical processing implemented in FREALIGN<sup>26</sup>. First,  
174 the model coordinates used for the averaging are based on the matrix of  $\alpha$ -tubulin  
175 monomers along a full turn rather than the single  $\alpha$ -tubulin monomer. Second, in the  
176 FREALIGN averaging approach the signal from the dimers at the seam are down-  
177 weighted, whereas NCS averaging allows us to separate the signal from the seam, and



178 thus to deconvolute the signal from the non-seam locations. Third, this procedure also  
179 acts to low-pass filter the map to 4 Å (the high-resolution limit of the C1 map,  
180 Supplemental Figure 5), which should suppress noise from the more disordered parts of  
181 the map, including alternative conformations of the  $\alpha$ K40 loop. Using this NCS-based  
182 approach, we were able to resolve density and build a model for three additional residues,  
183 the acetylated K40, T41, and I42. These residues pack towards the globular domain of  $\alpha$   
184 tubulin, consistent with the favorability of burying these relatively hydrophobic residues in  
185 the Ac<sup>96</sup> state. Despite observing only very weak density, we have modeled the glycine-  
186 rich region that extends into the lumen as a tight turn, which we note is only possible due  
187 to the expanded Ramachandran space accessible to glycine residues (Figure 2c). In  
188 contrast, and despite better global resolution, we did not observe any density consistent  
189 with a stable conformation of the loop in the Ac<sup>0</sup> map. Based on this result, which is  
190 consistent across the NCS-averaged and traditionally symmetrized maps, we did not build  
191 any additional residues into the Ac<sup>0</sup> density (Figure 2d).

192 ***Ensemble modeling of the loop in each state using density-restrained molecular***  
193 ***dynamics***

194 For regions that exhibit a high degree of disorder, like the  $\alpha$ K40 loop, a single,  
195 static structure is a poor description of the native state. Ensemble models can help to  
196 elucidate how populations of conformations change upon perturbations, such as post-  
197 translational modifications<sup>29,30</sup>. To derive an ensemble of conformations representing the  
198 Ac<sup>96</sup> and Ac<sup>0</sup> states, we used the atomic structure built into the Ac<sup>96</sup> map as the starting  
199 model to initiate metainference-based molecular dynamics (MD) simulations, which

200 augment a standard forcefield with a term representing the density derived from the EM  
201 map<sup>31</sup>. In contrast to Molecular Dynamics and Flexible Fitting (MDFF) and other  
202 refinement methods that seek to converge on a single structure<sup>32</sup>, this method models a  
203 structural ensemble by maximizing the collective agreement between simulated and  
204 experimental maps, and accounts for noise using a Bayesian approach<sup>33</sup>. Initiating  
205 simulations for both the Ac<sup>96</sup> and Ac<sup>0</sup> states from starting models that differ only in the  
206 acetyl group and distinct input experimental density maps allowed us to test whether  
207 acetylation restricts the motion of the loop, trapping it in a tighter ensemble of  
208 conformations.

209 To analyze the conformational dynamics of the loop, we analyzed the root mean  
210 square fluctuations of residues 36-48 within replicas for each simulation. This analysis  
211 shows that the  $\alpha$ K40 loop fluctuations are more restricted in the Ac<sup>96</sup> state than in the Ac<sup>0</sup>  
212 state (Figure 3a). Next, we analyzed the distribution of conformations adopted by the loop  
213 by analyzing the distance between K40 and the globular domain of  $\alpha$ -tubulin (represented  
214 by L26) and by clustering together the snapshots from all replicas of both simulations  
215 based on the root mean square deviations of residues 36-48. Similar to the starting  
216 reference model, where the distance is 10.6 Å, Ac<sup>96</sup> is enriched in conformations that  
217 pack close to the globular domain of the  $\alpha$ -tubulin core (Figure 3b). These conformations,  
218 exemplified by clusters 1, 4, and 6, position the acetylated lysine to interact with residues  
219 along H1. In contrast, the Ac<sup>0</sup> state favors conformations that extend towards the MT  
220 lumen, as exemplified by clusters 0, 2, 5, 7, and 8 (Figure 3b). Clusters 3, 9, 10, 11,  
221 labeled in grey, had equal numbers of frames enriched in Ac<sup>96</sup> and Ac<sup>0</sup> and sampled rare

222 (<5%) extreme states on both the exposed and packed ends of the conformational  
223 spectrum (Figure 3b).

224         These computational results are consistent with the visual analysis of the density  
225 for both the NCS and traditionally symmetrized maps, which indicated that the loop is  
226 more ordered after acetylation. The residual disorder identified by the simulations using  
227 the Ac<sup>96</sup> map may be important for de-acetylation by SIRT2. On the other hand, the  
228 increased flexibility we observe for the Ac<sup>0</sup> state suggests a potential mechanism by which  
229  $\alpha$ TAT1 could acetylate K40. Previous proposals argue that acetylation can occur from the  
230 outside or inside of the lumen<sup>25</sup>. However, to catalyze the modification, a flexible region  
231 within  $\alpha$ TAT1 would have to extend approximately 25 Å through a MT wall fenestration  
232 between four tubulin dimers to reach  $\alpha$ K40, or the MT would have to undergo a major  
233 structural rearrangement in the lattice to allow  $\alpha$ TAT1 to enter the lumen. Previous work  
234 demonstrated that the  $\alpha$ TAT1 active site and its MT recognition surface is concave and  
235 could not stretch through the lumen<sup>25</sup>. Our findings support the idea that  $\alpha$ TAT1 modifies  
236 the loop from within the lumen of the MT because the deacetylated loop samples  
237 extended structures that would be accessible to  $\alpha$ TAT1 and because the structural  
238 rearrangement caused by acetylation is small and local to the  $\alpha$ K40 loop.

239 ***Acetylation induces a local structural rearrangement of the  $\alpha$ K40 loop that***  
240 ***promotes stability by weakening lateral contacts***

241         Collectively our structural and MD results show that acetylation restricts the motion  
242 of the  $\alpha$ K40 loop. These results led us to hypothesize that the change in the structural  
243 ensemble of the  $\alpha$ K40 loop upon acetylation, while subtle and local, may affect lateral

244 contacts. These local changes may disrupt the small lateral interface between  $\alpha$ -tubulin  
245 subunits. The origin of this effect may be highly distributed, as we do not visualize any  
246 stable interactions between the Ac<sup>0</sup> state of the loop and the globular domain. However,  
247 upon acetylation, the structural ensemble becomes more restricted and the potential for  
248 the loop to strengthen any of these interactions between monomers is lost. For example,  
249 in many of the extended conformations favored by the Ac<sup>0</sup> state, K40 in a  $\alpha$ 1-monomer is  
250 close to the M-loop of the neighboring  $\alpha$ 2-monomer and may buttress the H1'-S2 loop,  
251 providing support for the vital  $\alpha$ 1K60: $\alpha$ 2H283 lateral interaction (Figure 4). In contrast, when  
252 K40 is acetylated it packs  $\sim 10$  Å closer to the globular domain of the  $\alpha$ 1-monomer,  
253 reducing the potential for inter-monomer interactions (Figure 4).

254 We tested whether the loss of the positive charge of the lysine upon acetylation  
255 alters the electrostatic interaction energy and the hydrogen-bonding network at the lateral  
256 interface using MD simulations based on the Debye-Hückel (DH) formula<sup>34,35</sup>. We found  
257 that acetylation does indeed weaken lateral interactions (Supplemental Figure 4).  
258 Additionally, the Ac<sup>0</sup> ensemble contains conformations with strong DH interaction  
259 energies that do not exist in the Ac<sup>96</sup> ensemble (Supplemental Figure 4). While the effects  
260 of acetylation are subtle, the local effects at the lateral contacts site may have an additive  
261 effect that stabilizes the MT lattice. This idea is consistent with previous work that argues  
262 that the weakening of lateral interactions is a protective mechanism to prevent pre-  
263 existing lattice defects from spreading into large areas of damage under repeated  
264 stress—a mechanism that could be exploited by cancer cells<sup>21,22</sup>.

265 In conclusion, this comprehensive approach combines the structural insight of  
266 cryoEM with the sampling efficiency and global scope of MD to investigate how PTMs  
267 can transform a conformational ensemble<sup>36,37</sup>. Our high-resolution maps serve as a  
268 blueprint for the scale of conformational change and relevant degrees-of-freedom that the  
269  $\alpha$ K40 loop can sample with all-atomistic metainference MD<sup>36</sup>. We show that  $\alpha$ TAT1  
270 induces a site-specific electrostatic perturbation that restricts the motion of the loop.  $\alpha$ K40  
271 acetylation may function as an evolutionarily conserved ‘electrostatic switch’ to regulate  
272 MT stability<sup>36,37</sup>.

273

## 274 **MATERIALS AND METHODS**

### 275 Sample Preparation for Cryo-Electron Microscopy

276 Porcine brain tubulin was purified as previously described<sup>38</sup> and reconstituted to 10 mg/ml  
277 in BRB80 buffer (80 mM 1,4-piperazinediethanesulfonic acid [PIPES], pH 6.9, 1 mM  
278 ethylene glycol tetraacetic acid [EGTA], 1 mM MgCl<sub>2</sub>) with 10% (vol/vol) glycerol, 1 mM  
279 GTP, and 1 mM DTT, and flash frozen in 10  $\mu$ l aliquots until needed. The acetylated and  
280 deacetylated MTs (15  $\mu$ M) were co-polymerized with end-binding protein 3 (EB3, 25  $\mu$ M),  
281 at 37°C for ~15 min in the presence of 10% NP-40, 1mM dithiothreitol (DTT), and BRB80  
282 buffer. The EB3 decorated MTs were added to glow-discharged C-flat holey carbon grids  
283 (CF-1.2/1.3-4C, 400 mesh, Copper; Protochips, Morrisville, NC) inside a Vitrobot (FEI,  
284 Hillsboro, OR) set at 37°C and 85% humidity before plunge-freezing in ethane slush and  
285 liquid nitrogen, respectively, as previously described<sup>2</sup>.

### 286 Cryo-Electron Microscopy

287 Micrographs were collected using a Titan Krios microscope (Thermo Fisher Scientific,  
288 Inc., Waltham, MA) operated at an accelerating voltage of 300 kV. All cryo-EM images  
289 were recorded on a K2 Summit direct electron detector (Gatan, Pleasanton, CA), at a  
290 nominal magnification of x22,500, corresponding to a calibrated pixel size of 1.07 Å. The  
291 camera was operated in super-resolution mode, with a dose rate of  $\sim 2$  e<sup>-</sup> per pixel per s  
292 on the detector. We used a total exposure time of 4 s, corresponding to a total dose of 25  
293 electrons/Å<sup>2</sup> on the specimen. The data were collected semi-automatically using the  
294 SerialEM software suite<sup>39</sup>.

### 295 Image Processing

296 Stacks of dose-fractionated image frames were aligned using the UCSF MotionCor2  
297 software<sup>40</sup>. MT segments were manually selected from the drift-corrected images  
298 (acetylated dataset: 205 images, deacetylated MT dataset: 476 images) using the  
299 APPION image processing suite<sup>41</sup>. We estimated the CTF using CTFFIND4<sup>42</sup> and  
300 converted the segments to 90% overlapping boxes (512 × 512 pixels) for particle  
301 extraction. The remaining non-overlapping region is set to 80 Å and corresponds to the  
302 tubulin dimer repeat (asymmetric unit). Consequently, there are  $\sim 13$  unique tubulin  
303 dimers per MT particle. To determine the initial global alignment parameters and PF  
304 number for each MT particle, raw particles were compared to 2D projections of low-  
305 passed filtered MT models ( $\sim 20$  Å, 4° coarse angular step size) with 12, 13, 14 and 15  
306 PFs<sup>43</sup> using the multi-reference alignment (MSA) feature of EMAN1<sup>44</sup>. Finally, 13-PF MT  
307 particles (acetylated dataset: 20,256 particles, deacetylated MT dataset: 29,396) were  
308 refined in FREALIGN v. 9.11<sup>45,46</sup> using pseudo-helical symmetry to account for the

309 presence of the seam. To verify the location of the seam, we used the 40 Å shift approach  
310 to categorize MTs based on their azimuthal angle, as previously described<sup>27</sup>.

### 311 Atomic Model Building and Coordinate Refinement

312 COOT<sup>47</sup> was used to build the missing polypeptides of the  $\alpha$ K40 loop in  $\alpha$ -tubulin, using  
313 the available PDB 3JAR as a starting model. Successively, all novel atomic models were  
314 iteratively refined with `phenix.real_space_refine` into EM maps sharpened with  
315 `phenix.autosharpen`<sup>28,48</sup>. For visual comparisons between states, potential density  
316 thresholds were interactively adjusted in Coot to maximize iso-contour similarity around  
317 backbone atoms distant from the  $\alpha$ K40 loop. For Figures 1 & 2, all densities are  
318 represented in Chimera at a threshold of 1.1.

### 319 Molecular Dynamics Simulations

320 Code for map preparation, simulation execution, and analysis is available at:  
321 [https://github.com/fraser-lab/plumed\\_em\\_md](https://github.com/fraser-lab/plumed_em_md)

322 To prepare the cryoEM maps, we fitted the maps with a Gaussian Mixture Model (GMM)  
323 by applying a divide-and-conquer approach<sup>33</sup>, using `generate_gmm.py` and  
324 `convert_GMM2PLUMED.sh`. Cross-correlations to the experimental maps were greater  
325 than 0.99. All simulations were performed with GROMACS 2016.5<sup>34</sup> and the PLUMED-  
326 ISDB module<sup>49</sup> of the PLUMED library<sup>50</sup> using the Charmm36-jul2017 forcefield<sup>51</sup> with  
327 patches for acetylated lysine (aly)<sup>52</sup> and the TIP3P water model. For the deacetylated  
328 simulations, the same starting model was used with a manual edit of the PDB to eliminate  
329 the acetylation (with all hydrogens replaced by GROMACS during model preparation).  
330 The initial model was minimized then equilibrated for 2ns, using `prep_plumed.py`. MD  
331 simulations were performed on a metainference ensemble of 8 replicas for an aggregate

332 simulation time of 96ns for each acetylation state, using prep\_plumed2.py and  
333 prep\_plumed3.py. Contributions of negative scatterers (atoms OD1 and OD2 of Asp  
334 residues; OE1 and OE2 of Glu) were excluded from contributing to the predicted maps  
335 during the simulation. This modification effectively eliminates the contribution of these  
336 side chains to the agreement between density maps, in keeping with the non-existent  
337 density of negatively charged side chains in EM maps, while allowing them to contribute  
338 to the simulation through the energy function. Clustering and convergence analyses<sup>31</sup>  
339 were performed and analyzed using MDAnalysis<sup>53</sup>.

340 Changes in the electrostatic interaction energies at the lateral contacts were  
341 determined using the using the Debye-Hückel (DH) formula:

$$346 \quad \frac{1}{4\pi\epsilon_r\epsilon_0} \sum_{i \in A} \sum_{j \in B} q_i q_j \frac{e^{-\kappa|r_{ij}|}}{|r_{ij}|}$$

342 where  $\epsilon_0$  is the vacuum's dielectric constant,  $\epsilon_r$  the dielectric constant of the solvent,  $q_i$   
343 and  $q_j$  the charges of the  $i$ -th and  $j$ -th atoms, respectively,  $|r_{ij}|$  the distance between  
344 these two atoms, and  $\kappa$  is the DH parameter<sup>35</sup> defined in terms of the temperature  $T$   
345 and the ionic strength of the solution  $I_S$ .

347 The DH energy is calculated between the following two groups of atoms, denoted  
348 as A and B in the formula above: (i) all atoms in residue range 30-60 of chain A ( $\alpha 1$   
349 subunit) and (ii) all atoms in residue range 200-380 of chain E ( $\alpha 2$  subunit) in PDBs  
350 **XXYA** and **XXYB**. Residues not included in this range do not significantly contribute to  
351 the DH interaction energy between adjacent  $\alpha$ -subunits. Parameters used in the  
352 calculation of the DH energy are: temperature ( $T=300\text{K}$ ), dielectric constant of solvent  
353 ( $\epsilon_r=80$ ; water at room temperature), and ionic strength ( $I_S=1\text{M}$ ).



354

355 **ACCESSION NUMBERS**

356 All electron density maps have been deposited in the EMDB accession numbers **EMD-**  
357 **X1, EMD-X2, EMD-X3, and EMD-X4**. Atomic models are deposited in the PDB accession  
358 numbers **XXYA, XXYB, XXYC, and XXYD, XXYE**.

359 **AUTHOR CONTRIBUTIONS**

360 D.P. performed the tubulin purification and modification to generate the Ac<sup>0</sup> and Ac<sup>96</sup>  
361 samples. L.E., R.Z., and D.T. performed the cryo-EM sample preparation, electron  
362 microscopy and data processing. L.E. and J.S.F. engineered the NCS-averaging  
363 technique, performed iterative model-building/refinement. L.E., J.S.F., T. L., M. V. and  
364 M.B. executed the metainference MD simulations. All authors contributed to structure  
365 interpretation, model development and manuscript writing.

366

367 **ACKNOWLEDGEMENTS**

368 We thank P. Grob and J. Fang for cryo-EM data collection support, A. Chintangal and P.  
369 Tobias for computational support, and E. Kellogg, B. LaFrance, S. Howes, T.H.D.  
370 Nguyen, S. Pöpsel, B. Greber, and K. Morris for helpful discussions. We also  
371 acknowledge the Berkeley Bay Area Cryo-EM (BACEM) Facility and additional scientific  
372 resources at UC Berkeley. J.S.F was funded by the UCSF-UCB Sackler Faculty  
373 Exchange Program and NIGMS grant R01- GM123159. This work was funded through  
374 NIGMS grants R01-GM63072 to E.N. and the NSF grant 2016222703 and the NAS NRC  
375 Ford Foundation grant to L.E. E.N. is a Howard Hughes medical investigator.

376

## 377 REFERENCES

- 378 1. Nogales, E., Whittaker, M., Milligan, R. A. & Downing, K. H. High-resolution model  
379 of the microtubule. *Cell* (1999). doi:10.1016/S0092-8674(00)80961-7
- 380 2. Zhang, R., Alushin, G. M., Brown, A. & Nogales, E. Mechanistic origin of  
381 microtubule dynamic instability and its modulation by EB proteins. *Cell* (2015).  
382 doi:10.1016/j.cell.2015.07.012
- 383 3. Mitchison, T. J. Localization of an exchangeable GTP binding site at the plus end  
384 of microtubules. *Science* (80-. ). (1993). doi:10.1126/science.8102497
- 385 4. Mitchison, T. & Kirschner, M. Dynamic instability of microtubule growth. *Nature*  
386 (1984). doi:10.1038/312237a0
- 387 5. Walsh, G. & Jefferis, R. Post-translational modifications in the context of  
388 therapeutic proteins. *Nature Biotechnology* (2006). doi:10.1038/nbt1252
- 389 6. Magiera, M. M., Singh, P., Gadadhar, S. & Janke, C. Tubulin Posttranslational  
390 Modifications and Emerging Links to Human Disease. *Cell* (2018).  
391 doi:10.1016/j.cell.2018.05.018
- 392 7. Janke, C. & Montagnac, G. Causes and Consequences of Microtubule  
393 Acetylation. *Curr. Biol.* **27**, R1287–R1292 (2017).
- 394 8. Janke, C. & Bulinski, J. C. Post-translational regulation of the microtubule  
395 cytoskeleton: Mechanisms and functions. *Nature Reviews Molecular Cell Biology*  
396 (2011). doi:10.1038/nrm3227
- 397 9. Howes, S. C., Alushin, G. M., Shida, T., Nachury, M. V. & Nogales, E. Effects of  
398 tubulin acetylation and tubulin acetyltransferase binding on microtubule structure.  
399 *Mol. Biol. Cell* (2014). doi:10.1091/mbc.E13-07-0387
- 400 10. LeDizet, M. & Piperno, G. Identification of an acetylation site of Chlamydomonas  
401 alpha-tubulin. *Proc. Natl. Acad. Sci.* (1987). doi:10.1073/pnas.84.16.5720
- 402 11. LeDizet, M. & Piperno, G. Cytoplasmic microtubules containing acetylated  $\alpha$ -  
403 tubulin in Chlamydomonas reinhardtii: Spatial arrangement and properties. *J. Cell*  
404 *Biol.* (1986). doi:10.1083/jcb.103.1.13
- 405 12. De Brabander, M. J., Van de Veire, R. M. L., Aerts, F. E. M., Borgers, M. &  
406 Janssan, P. A. J. The Effects of Methyl [5-(2-Thienylcarbonyl)-1H-benzimidazol-2-  
407 yl]carbamate, (R 17934; NSC 238159), a New Synthetic Antitumoral Drug  
408 Interfering with Microtubules, on Mammalian Cells Cultured in Vitro. *Cancer Res.*  
409 (1976).
- 410 13. Dompierre, J. P. *et al.* Histone Deacetylase 6 Inhibition Compensates for the  
411 Transport Deficit in Huntington's Disease by Increasing Tubulin Acetylation. *J.*  
412 *Neurosci.* (2007). doi:10.1523/JNEUROSCI.0037-07.2007
- 413 14. D'Ydewalle, C. *et al.* HDAC6 inhibitors reverse axonal loss in a mouse model of  
414 mutant HSPB1-induced Charcot-Marie-Tooth disease. *Nat. Med.* (2011).  
415 doi:10.1038/nm.2396
- 416 15. Kim, J. Y. *et al.* HDAC6 Inhibitors Rescued the Defective Axonal Mitochondrial  
417 Movement in Motor Neurons Derived from the Induced Pluripotent Stem Cells of  
418 Peripheral Neuropathy Patients with HSPB1 Mutation. *Stem Cells Int.* (2016).  
419 doi:10.1155/2016/9475981

- 420 16. Li, L. *et al.* MEC-17 Deficiency Leads to Reduced  $\alpha$ -Tubulin Acetylation and  
421 Impaired Migration of Cortical Neurons. *J. Neurosci.* (2012).  
422 doi:10.1523/JNEUROSCI.0016-12.2012
- 423 17. Godena, V. K. *et al.* Increasing microtubule acetylation rescues axonal transport  
424 and locomotor deficits caused by LRRK2 Roc-COR domain mutations. *Nat.*  
425 *Commun.* (2014). doi:10.1038/ncomms6245
- 426 18. Boggs, A. E. *et al.*  $\alpha$ -Tubulin acetylation elevated in metastatic and basal-like  
427 breast cancer cells promotes microtentacle formation, adhesion, and invasive  
428 migration. *Cancer Res.* (2015). doi:10.1158/0008-5472.CAN-13-3563
- 429 19. Di Martile, M., Del Bufalo, D. & Trisciuglio, D. The multifaceted role of lysine  
430 acetylation in cancer: prognostic biomarker and therapeutic target. *Oncotarget*  
431 (2015). doi:10.18632/oncotarget.10048
- 432 20. Maruta, H., Greer, K. & Rosenbaum, J. L. The acetylation of alpha-tubulin and its  
433 relationship to the assembly and disassembly of microtubules. *J. Cell Biol.* (1986).  
434 doi:10.1083/jcb.103.2.571
- 435 21. Portran, D., Schaedel, L., Xu, Z., Théry, M. & Nachury, M. V. Tubulin acetylation  
436 protects long-lived microtubules against mechanical ageing. **19**, (2017).
- 437 22. Xu, Z. *et al.* Microtubules acquire resistance from mechanical breakage through  
438 intraluminal acetylation. *Science (80- )*. (2017). doi:10.1126/science.aai8764
- 439 23. Cueva, J. G., Hsin, J., Huang, K. C. & Goodman, M. B. Posttranslational  
440 acetylation of  $\alpha$ -tubulin constrains protofilament number in native microtubules.  
441 *Curr. Biol.* (2012). doi:10.1016/j.cub.2012.05.012
- 442 24. Chaaban, S. & Brouhard, G. J. A microtubule bestiary: structural diversity in  
443 tubulin polymers. *Mol. Biol. Cell* **28**, 2924–2931 (2017).
- 444 25. Szyk, A. *et al.* Molecular basis for age-dependent microtubule acetylation by  
445 tubulin acetyltransferase. *Cell* (2014). doi:10.1016/j.cell.2014.03.061
- 446 26. Alushin, G. M. *et al.* High-Resolution microtubule structures reveal the structural  
447 transitions in  $\alpha\beta$ -tubulin upon GTP hydrolysis. *Cell* (2014).  
448 doi:10.1016/j.cell.2014.03.053
- 449 27. Zhang, R. & Nogales, E. A new protocol to accurately determine microtubule  
450 lattice seam location. *J. Struct. Biol.* (2015). doi:10.1016/j.jsb.2015.09.015
- 451 28. Adams, P. D. *et al.* PHENIX: A comprehensive Python-based system for  
452 macromolecular structure solution. *Acta Crystallogr. Sect. D Biol. Crystallogr.*  
453 (2010). doi:10.1107/S0907444909052925
- 454 29. Bonomi, M. & Vendruscolo, M. Determination of protein structural ensembles  
455 using cryo-electron microscopy. 1–22 (2018).
- 456 30. Vahidi, S. *et al.* Reversible inhibition of the ClpP protease via an N-terminal  
457 conformational switch. *Proc. Natl. Acad. Sci.* (2018).  
458 doi:10.1073/pnas.1805125115
- 459 31. Bonomi, M., Pellarin, R. & Vendruscolo, M. Simultaneous Determination of  
460 Protein Structure and Dynamics Using Cryo-Electron Microscopy. *Biophys. J.*  
461 (2018). doi:10.1016/j.bpj.2018.02.028
- 462 32. Singharoy, A. *et al.* Molecular dynamics-based refinement and validation for sub-5  
463 Å cryo-electron microscopy maps. *Elife* (2016). doi:10.7554/eLife.16105
- 464 33. Hanot, S. *et al.* Multi-scale Bayesian modeling of cryo-electron microscopy  
465 density maps. *bioRxiv* (2017). doi:10.1101/113951

- 466 34. Hess, B., Kutzner, C., Van Der Spoel, D. & Lindahl, E. GRGMACS 4: Algorithms  
467 for highly efficient, load-balanced, and scalable molecular simulation. *J. Chem.*  
468 *Theory Comput.* (2008). doi:10.1021/ct700301q
- 469 35. Do, T. N., Carloni, P., Varani, G. & Bussi, G. RNA/peptide binding driven by  
470 electrostatics - Insight from bidirectional pulling simulations. *J. Chem. Theory*  
471 *Comput.* (2013). doi:10.1021/ct3009914
- 472 36. Narayanan, A. & Jacobson, M. P. Computational studies of protein regulation by  
473 post-translational phosphorylation. *Current Opinion in Structural Biology* (2009).  
474 doi:10.1016/j.sbi.2009.02.007
- 475 37. Beltrao, P. *et al.* Evolution and functional cross-talk of protein post-translational  
476 modifications. *Mol. Syst. Biol.* (2013). doi:10.1002/msb.201304521
- 477 38. Castoldi, M. & Popov, A. V. Purification of brain tubulin through two cycles of  
478 polymerization- depolymerization in a high-molarity buffer. *Protein Expr. Purif.*  
479 (2003). doi:10.1016/S1046-5928(03)00218-3
- 480 39. Mastronarde, D. N. Automated electron microscope tomography using robust  
481 prediction of specimen movements. *J. Struct. Biol.* (2005).  
482 doi:10.1016/j.jsb.2005.07.007
- 483 40. Zheng, S., Palovcak, E., Armache, J.-P., Cheng, Y. & Agard, D. Anisotropic  
484 Correction of Beam-induced Motion for Improved Single-particle Electron Cryo-  
485 microscopy. *bioRxiv* (2016). doi:10.1101/061960
- 486 41. Lander, G. C. *et al.* Appion: An integrated, database-driven pipeline to facilitate  
487 EM image processing. *J. Struct. Biol.* (2009). doi:10.1016/j.jsb.2009.01.002
- 488 42. Rohou, A. & Grigorieff, N. CTFFIND4: Fast and accurate defocus estimation from  
489 electron micrographs. *J. Struct. Biol.* (2015). doi:10.1016/j.jsb.2015.08.008
- 490 43. Egelman, E. H. The iterative helical real space reconstruction method:  
491 Surmounting the problems posed by real polymers. *J. Struct. Biol.* (2007).  
492 doi:10.1016/j.jsb.2006.05.015
- 493 44. Ludtke, S. J., Baldwin, P. R. & Chiu, W. EMAN: Semiautomated software for high-  
494 resolution single-particle reconstructions. *J. Struct. Biol.* (1999).  
495 doi:10.1006/j.sbi.1999.4174
- 496 45. Lyumkis, D., Brilot, A. F., Theobald, D. L. & Grigorieff, N. Likelihood-based  
497 classification of cryo-EM images using FREALIGN. *J. Struct. Biol.* (2013).  
498 doi:10.1016/j.jsb.2013.07.005
- 499 46. Grigorieff, N. FREALIGN: High-resolution refinement of single particle structures.  
500 *J. Struct. Biol.* (2007). doi:10.1016/j.jsb.2006.05.004
- 501 47. Emsley, P., Lohkamp, B., Scott, W. G. & Cowtan, K. Features and development of  
502 Coot. *Acta Crystallogr. Sect. D Biol. Crystallogr.* (2010).  
503 doi:10.1107/S0907444910007493
- 504 48. Terwilliger, T. C. *et al.* Automated map sharpening by maximization of detail and  
505 connectivity Bioscience Division , Los Alamos National Laboratory , Mail Stop  
506 M888 , Los Alamos , NM , Molecular Biophysics and Integrated Bioimaging  
507 Division , Lawrence Berkeley National. (2018).
- 508 49. Bonomi, M. & Camilloni, C. Integrative structural and dynamical biology with  
509 PLUMED-ISDB. *Bioinformatics* (2017). doi:10.1093/bioinformatics/btx529
- 510 50. Tribello, G. A., Bonomi, M., Branduardi, D., Camilloni, C. & Bussi, G. PLUMED 2:  
511 New feathers for an old bird. *Comput. Phys. Commun.* (2014).

- 512           doi:10.1016/j.cpc.2013.09.018  
513   51.   Huang, J. & Mackerell, A. D. CHARMM36 all-atom additive protein force field:  
514       Validation based on comparison to NMR data. *J. Comput. Chem.* (2013).  
515       doi:10.1002/jcc.23354  
516   52.   Huang, J. *et al.* CHARMM36m: An improved force field for folded and intrinsically  
517       disordered proteins. *Nat. Methods* (2016). doi:10.1038/nmeth.4067  
518   53.   Michaud-Agrawal, N., Denning, E. J., Woolf, T. B. & Beckstein, O. MDAAnalysis: A  
519       toolkit for the analysis of molecular dynamics simulations. *J. Comput. Chem.*  
520       (2011). doi:10.1002/jcc.21787  
521  
522  
523  
524  
525  
526

527 **FIGURE LEGENDS**

528

529 **Figure 1. High-resolution maps of 96% acetylated (Ac<sup>96</sup>) and <1% acetylated (Ac<sup>0</sup>)**

530 **microtubules. (a)** Schematic of the model-building and refinement process in PHENIX.

531 We sharpened a representative 4x3 lattice, refined the corresponding atomic structure

532 (3JAR) into our map, and extracted out the central dimer to build additional residues into

533 the  $\alpha$ K40 loop. We performed this process iteratively for both the Ac<sup>96</sup> and Ac<sup>0</sup>. The

534 structure of the Ac<sup>96</sup> **(b)** and Ac<sup>0</sup> **(c)**  $\alpha\beta$ -tubulin heterodimers, respectively, are shown from

535 the outer and luminal views with close-ups of  $\alpha$ K40 loop in each state **(d)** and **(e)** low-

536 pass filtered to 3.7 Å.

537

538 **Figure 2. Symmetrized and NCS-averaged C1 maps of Ac<sup>96</sup> and Ac<sup>0</sup> microtubules**

539 **reveal the  $\alpha$ K40 loop is more ordered in the Ac<sup>96</sup> state.** Close-up views of the  $\alpha$ K40

540 loop (P37-D47) in the **(a)** Ac<sup>96</sup> and **(b)** Ac<sup>0</sup> states in the symmetrized maps low-pass

541 filtered to 4 Å and the **(c)** Ac<sup>96</sup> and **(d)** Ac<sup>0</sup> states in the NCS averaged C1 maps low-pass

542 filtered to 4 Å. Dotted lines indicate missing residues.

543

544 **Figure 3. Acetylation restricts the motion and alters the conformational ensemble**

545 **of the  $\alpha$ K40 loop.** (a) Per-residue root mean square fluctuations (RMSF) analyses were

546 determined over the course of 12 ns for residues 34-50 the C1 maps using GROMACS in

547 PLUMED and graphed using the MDAnalysis. (b) Ensemble modeling of the loop across

548 Ac<sup>96</sup> and Ac<sup>0</sup> states using density restrained MD. Frames were classified into one of 11

549 clusters by conformation. Clusters either had a greater number of Ac<sup>96</sup> frames (red), Ac<sup>0</sup>

550 frames (blue), or an equal number of frames from both states (grey). The reference is

551 shown in green. The unique conformations of each of the 11 clusters are shown to the  
552 right.

553

554 **Figure 4. Acetylation may weaken lateral interactions.** Close-up view of the lateral  
555 contacts between two  $\alpha$ -tubulin monomers at a non-seam location ( $\alpha$ 1, light green;  $\alpha$ 2,  
556 dark green). K40 in  $\alpha$ 1 of the Ac<sup>0</sup> state is 8 Å closer to the M-loop of  $\alpha$ 2 and appears to  
557 buttress the H1'-S2 loop, providing support for the vital  $\alpha$ 1K60- $\alpha$ 2H283 lateral interaction.  
558 By contrast, that support is lost in the Ac<sup>96</sup> state because the acetylated K40 now packs  
559 much closer to the hydrophobic, inner core.

560

561 **Supplemental Figure 1. Schematic of the experimental workflow for sample**  
562 **preparation and pseudo-helical image processing.** EB3 decorated MTs were added  
563 to glow-discharged C-flat holey carbon grids (CF-1.2/1.3-4C, 400 mesh, Copper;  
564 Protochips, Morrisville, NC) inside a Vitrobot (FEI, Hillsboro, OR) set at 37°C and 85%  
565 humidity before plunge-freezing in ethane slush and liquid nitrogen. Images were  
566 collected with the Titan Krios electron microscope (Thermo Fisher Scientific, Inc.,  
567 Waltham, MA) operated at 300kV and equipped with a K2 direct detector (Gatan,  
568 Pleasanton, CA). The micrographs were collected at a nominal magnification of  
569 x22,500. Stacks of dose-fractionated image frames were aligned using the UCSF  
570 MotionCor2 software and CTF-corrected with CTFFIND4. MT segments were manually  
571 selected and converted to 90% overlapping boxes (512 × 512 pixels) for particle  
572 extraction. The remaining non-overlapping region is set to 80 Å and corresponds to the  
573 tubulin dimer repeat (asymmetric unit). These raw particles were compared to 2D

574 projections of low-passed filtered MT models ( $\sim 20$  Å,  $4^\circ$  coarse angular step size) with  
575 13 and 14 PFs using the multi-reference alignment (MRA) feature of EMAN1. Next, 13-  
576 PF MT particles were refined in FREALIGN v. 9.11 using pseudo-helical symmetry to  
577 account for the presence of the seam. To verify the location of the seam, MTs were  
578 categorized based on their azimuthal angle and refined again.

579

### 580 **Supplemental Figure 2. Sample preparation, data collection and image**

581 **processing of acetylated and deacetylated MT samples. (a)** Ac<sup>96</sup> and Ac<sup>0</sup> tubulin

582 preparations were produced by treating purified mammalian brain tubulin (Ac<sup>30</sup>) with  
583 acetyltransferase  $\alpha$ TAT1 and deacetylase SIRT2. Samples were resolved on SDS-

584 page and Coomassie-stained (top panel) or immunoblotted for  $\alpha$ K40 acetylation (bottom

585 panel). Axomenal preparations from Tetrahymena cilia provide a 100% acetylation

586 calibrator. Adapted from Portran<sup>21</sup>. **(b)** Representative cryo-EM images of acetylated, in

587 the left panel, and deacetylated MTs, in the right panel. Scale bar = 200 nm. Images

588 were collected with the Titan Krios electron microscope (FEI, Hillsboro, OR) operated at

589 300kV and equipped with a K2 direct detector (Gatan, Pleasanton, CA). The

590 micrographs were collected at a nominal magnification of 22,500x, resulting in a final

591 pixel size of 1.07 Å per pixel and dose rate of 8 e-/pixel/s. **(c)** Schematic of data

592 collection. Using EB3, we generated >80% homogeneous samples to push the

593 resolution to  $\sim 3.5$  Å.

594

### 595 **Supplemental Figure 3. Previous proposed $\alpha$ K40 loop models. (a)** Published PDBs

596 with incomplete models of the loop: 5NQU (Chain A), 5EYP (Chain A), 3RYC (Chain A),



597 3RYC (Chain C), 5NQT (Chain A), 3RYI (Chain A), 3RYI (Chain A), 3RYF (Chain A),  
598 3RYF (Chain C). **(b)** Example of the a published PDB with the complete loop stabilized  
599 by calcium: 5YL4 (Chain C).

600

601 **Supplemental Figure 4. Acetylation weakens lateral interactions.** By analyzing the  
602 distribution of Debye-Hückel (DH) electrostatic energy between adjacent  $\alpha$ -subunits  
603 across the AC0 (blue) and AC96 ensembles (red), we find that acetylation weakens  
604 lateral interactions. The DH energy is calculated between the following two groups of  
605 atoms: (i) all atoms in residue range 30-60 of chain A ( $\alpha$ 1 subunit) and (ii) all atoms in  
606 residue range 200-380 of chain E ( $\alpha$ 2 subunit) in PDBs XXYA and XXYB. The plot  
607 shows the probability density function, or Pdf, as a function of the DH interaction  
608 energy.

609

610 **Supplemental Figure 5. Fourier Shell Correlation Plots.**

611 The  $FSC_{\text{half-map}}$  resolution, using **0.143** as the gold standard criterion, represents how  
612 well the two half-maps from each dataset correlate as a function of spatial frequency.  
613 The two half-maps were generated by dividing the final dataset into two independent  
614 3D-reconstructions. The  $FSC_{\text{map vs. model}}$  resolution, using **0.5** as the gold standard  
615 criterion, represents how well the final map correlated with the refined atomic model. All  
616 plots were generated in PHENIX.

617

618

619 **SUPPLEMENTAL TABLE 1. CryoEM data collection, refinement parameters, and**  
 620 **validation statistics.**

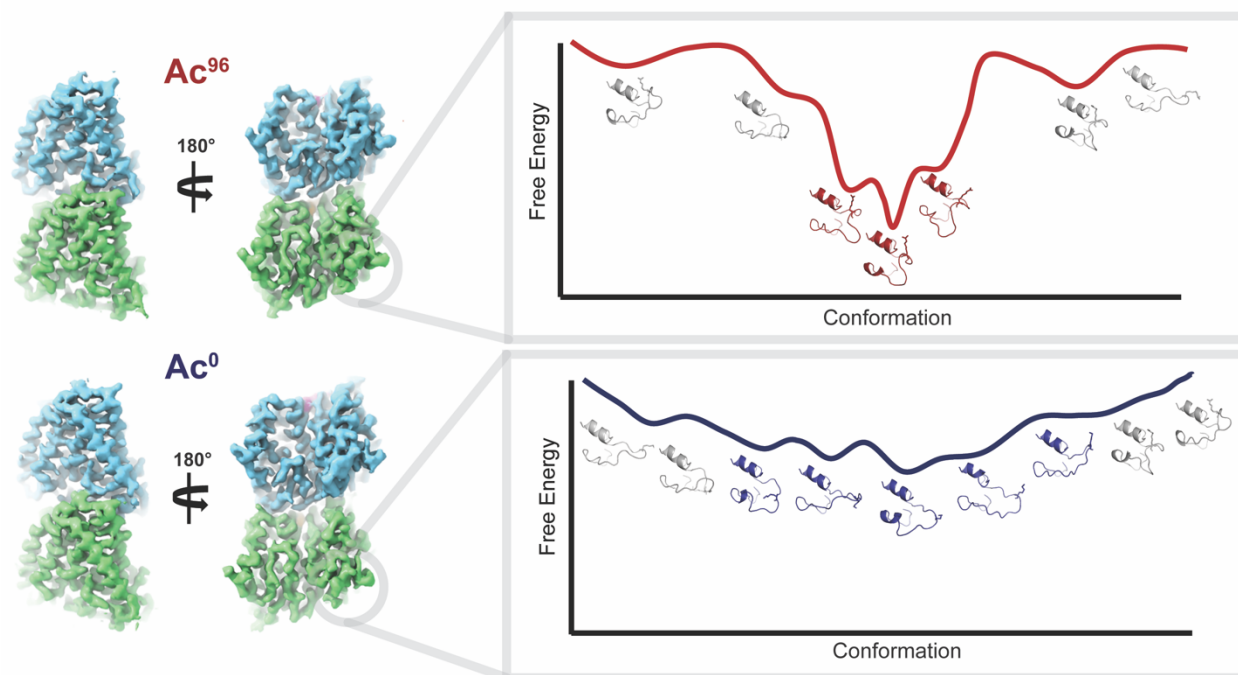
<b>Parameters</b>	<b>Ac<sup>96</sup> Symmetrized (EMDB-#, PDB-#)</b>	<b>Ac<sup>0</sup> Symmetrized (EMDB-#, PDB-#)</b>	<b>Ac<sup>96</sup> C1 (EMDB-#, PDB-#)</b>	<b>Ac<sup>0</sup> C1 (EMDB-#, PDB-#)</b>
Magnification	22500x	22500x	22500x	22500x
Voltage	300	300	300	300
Electron exposure (e- /Å <sup>2</sup> )	25	25	25	25
Defocus range (µm)	-1.5 to -2.5	-1.5 to -2.5	-1.5 to -2.5	-1.5 to -2.5
Pixel size (Å)	1.07 Å	1.07 Å	1.07 Å	1.07 Å
Symmetry imposed	HP	HP	C1	C1
Initial particle images (no.)	20256	29396	20256	29396
Final particle images (no.)	18432	24692	18432	24692
Helical Rise			9.3	9.3
Helical Twist			27.7	27.7
Dimer Rise (Å)			80.5	81
Dimer Twist			-0.12°	-0.12°
<b>Map resolution (Å)</b>	<b>3.3</b>	<b>3.7</b>	<b>4.1</b>	<b>4.0</b>
FSC threshold	0.143	0.143	0.143	0.143
Map resolution range (Å)	3.5-4.1 Å	3.0-3.6 Å	3.8-5.4 Å	3.5-4.5 Å
<b>Refinement</b>				
Initial model used (PDB ID)	3JAR	3JAR	3JAR	3JAR

Model resolution (Å)	4 Å	3.6 Å	6 Å	5.8 Å
FSC threshold	0.5	0.5	0.5	0.5
Map sharpening method	<i>Phenix_auto_sharpen</i>	<i>Phenix_auto_sharpen</i>	<i>Phenix_auto_sharpen</i>	<i>Phenix_auto_sharpen</i>
<b>Model composition</b>				
Nonhydrogen atoms	40866	40866	320775	320775
Protein residues	5184	5184	40702	40702
Ligands (GTP, GDP)	12	12	94	94
<b>B factors (Å<sup>2</sup>)</b>				
Protein	126.11	96.80	193.47	161.40
Ligand	122.25	89.44	192.42	156.32
Bond lengths: RMS (deviation)	0.007	0.007	0.007	0.006
Bond angles: RMS (deviation)	1.110	1.107	1.110	1.112
<b>Validation</b>				
MolProbity score	1.57	1.63	1.80	1.78
Clashscore	6.64	6.64	9.15	8.92
Rotamer outliers (%)	0.14	0.41	0.14	0.14
<b>Ramachandran plot</b>				
Favored (%)	96.74	96.18	95.48	95.6
Outliers (%)	0	0	0	0

621

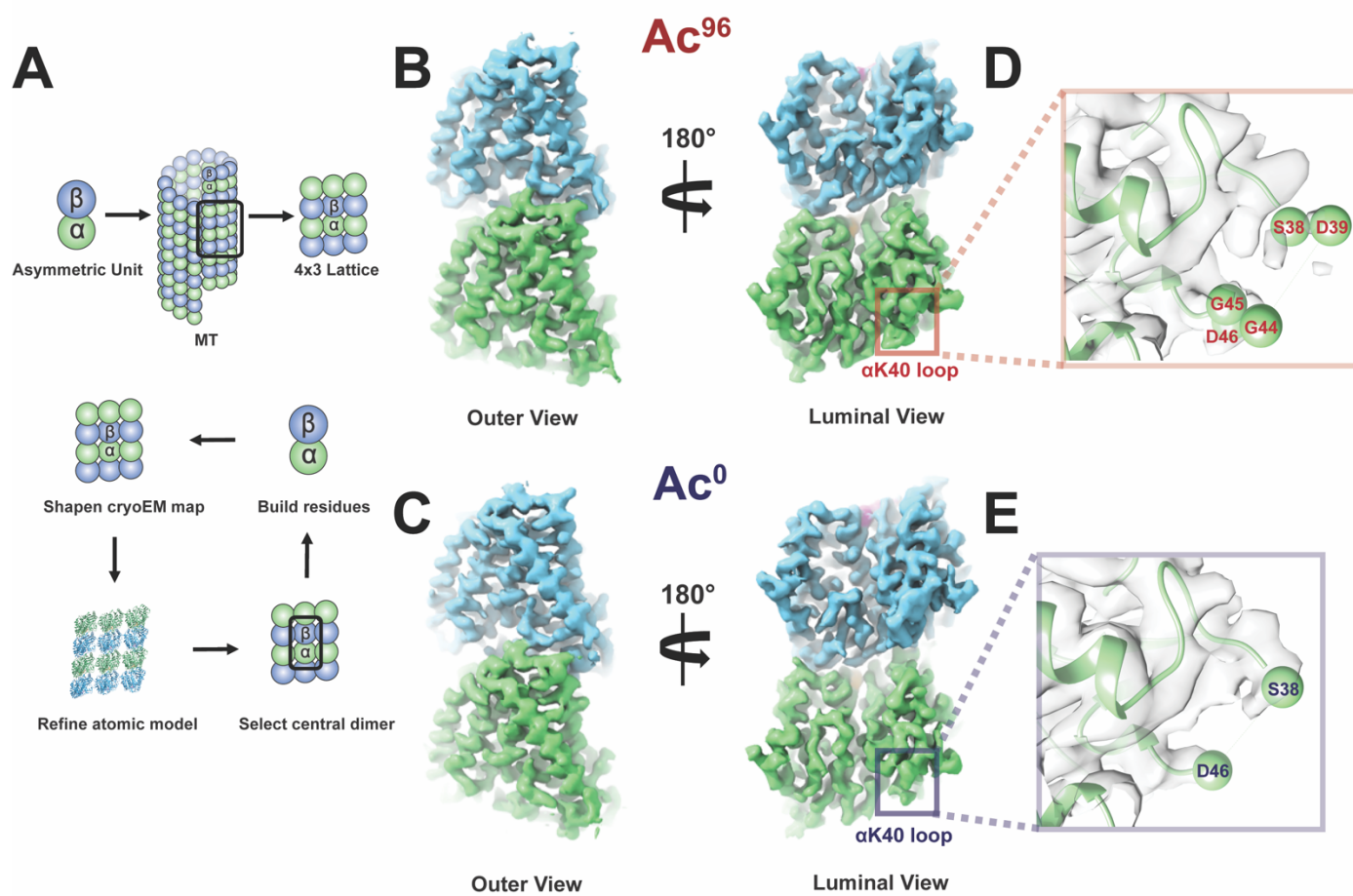
622

## GRAPHICAL ABSTRACT



623

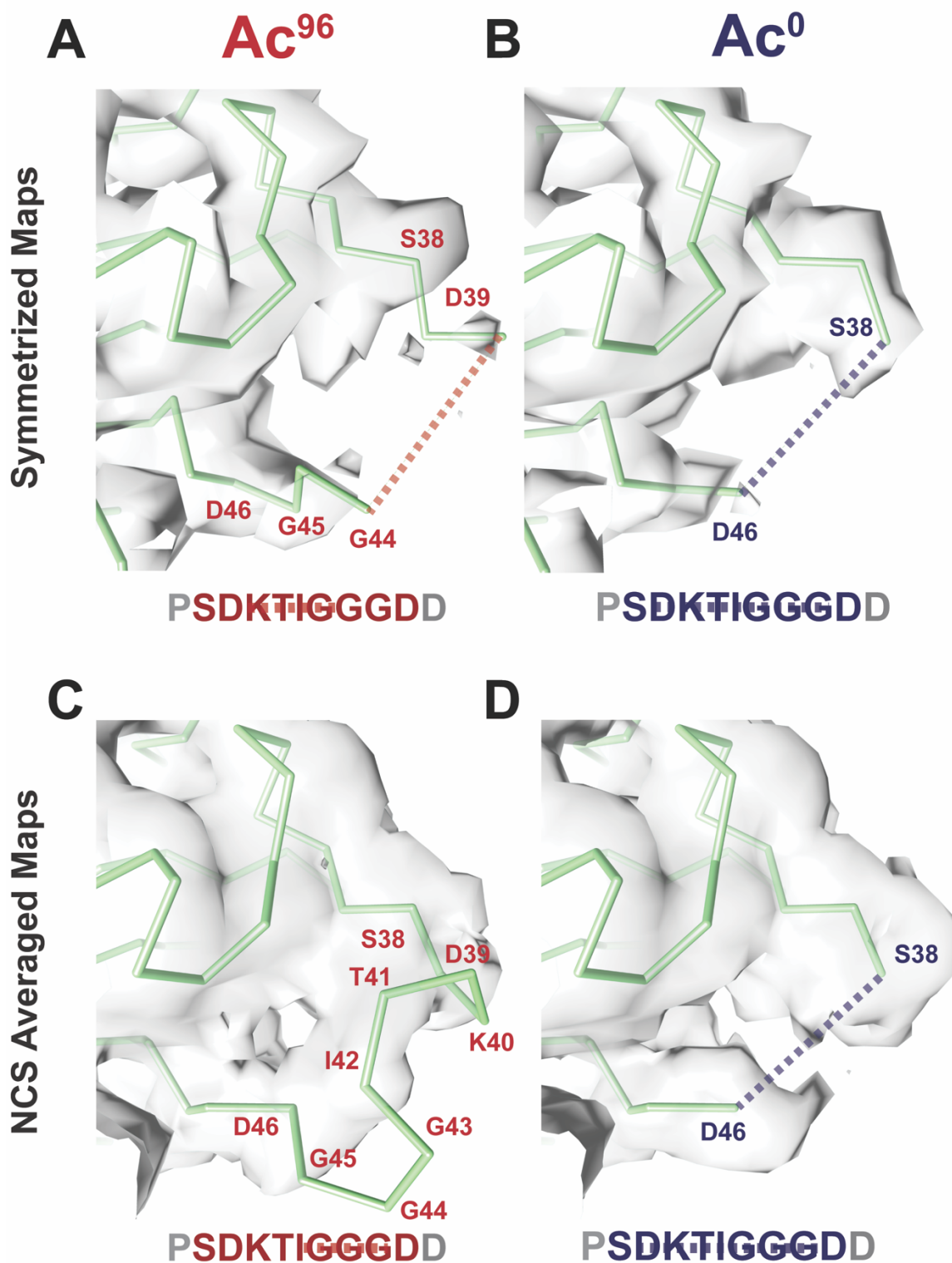
Acetylation alters the structural ensemble of the  $\alpha$ K40 loop of  $\alpha$ -tubulin.



624

625 **Figure 1. High-resolution maps of 96% acetylated ( $Ac^{96}$ ) and <1% acetylated ( $Ac^0$ )**

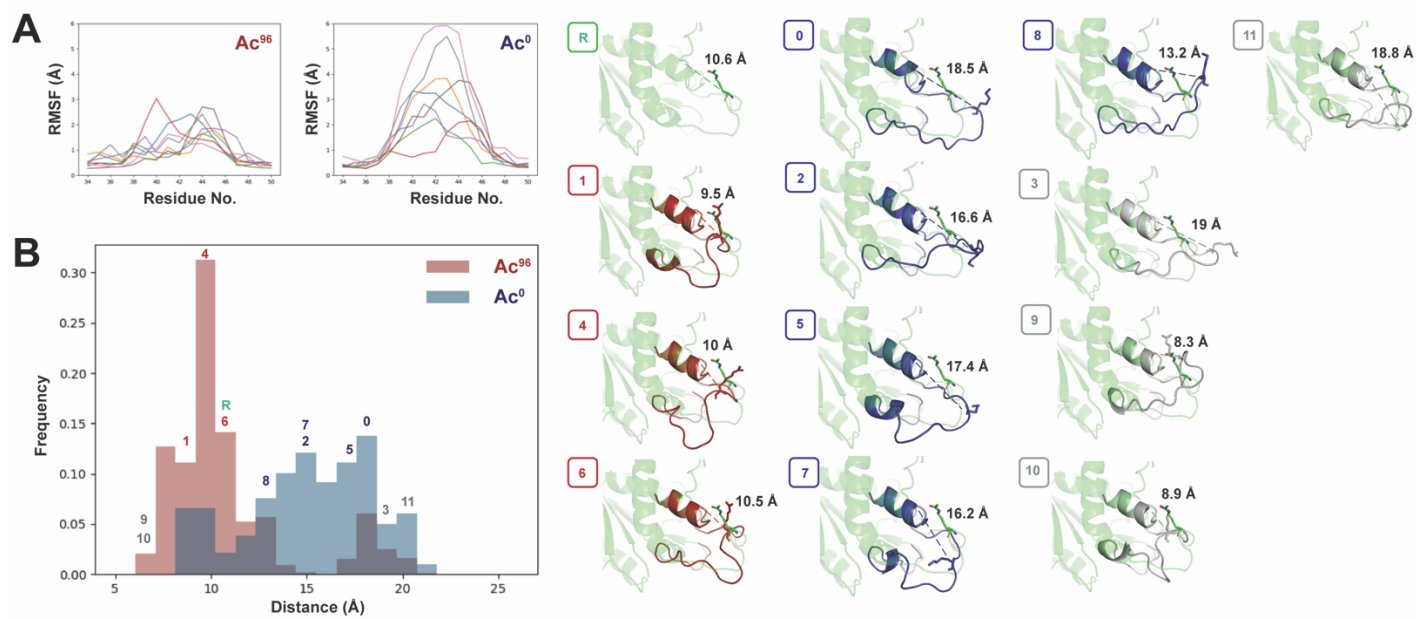
626 **microtubules.**



627

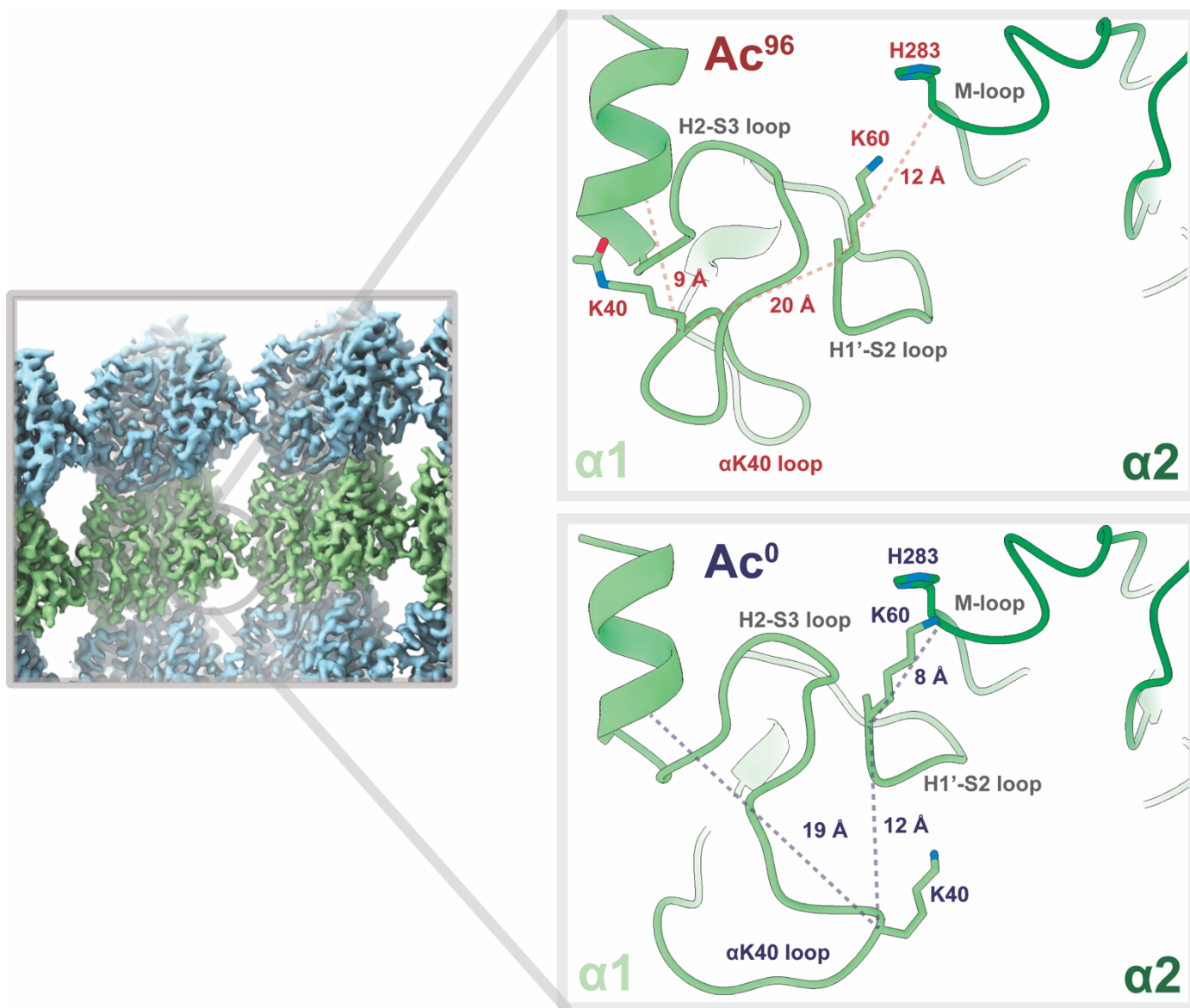
628 **Figure 2. Symmetrized and NCS-averaged C1 maps of Ac<sup>96</sup> and Ac<sup>0</sup> microtubules**

629 **reveal the  $\alpha$ K40 loop is more ordered in the Ac<sup>96</sup> state.**



630

631 **Figure 3. Acetylation restricts the motion and alters the conformational ensemble**  
632 **of the  $\alpha$ K40 loop.**



633

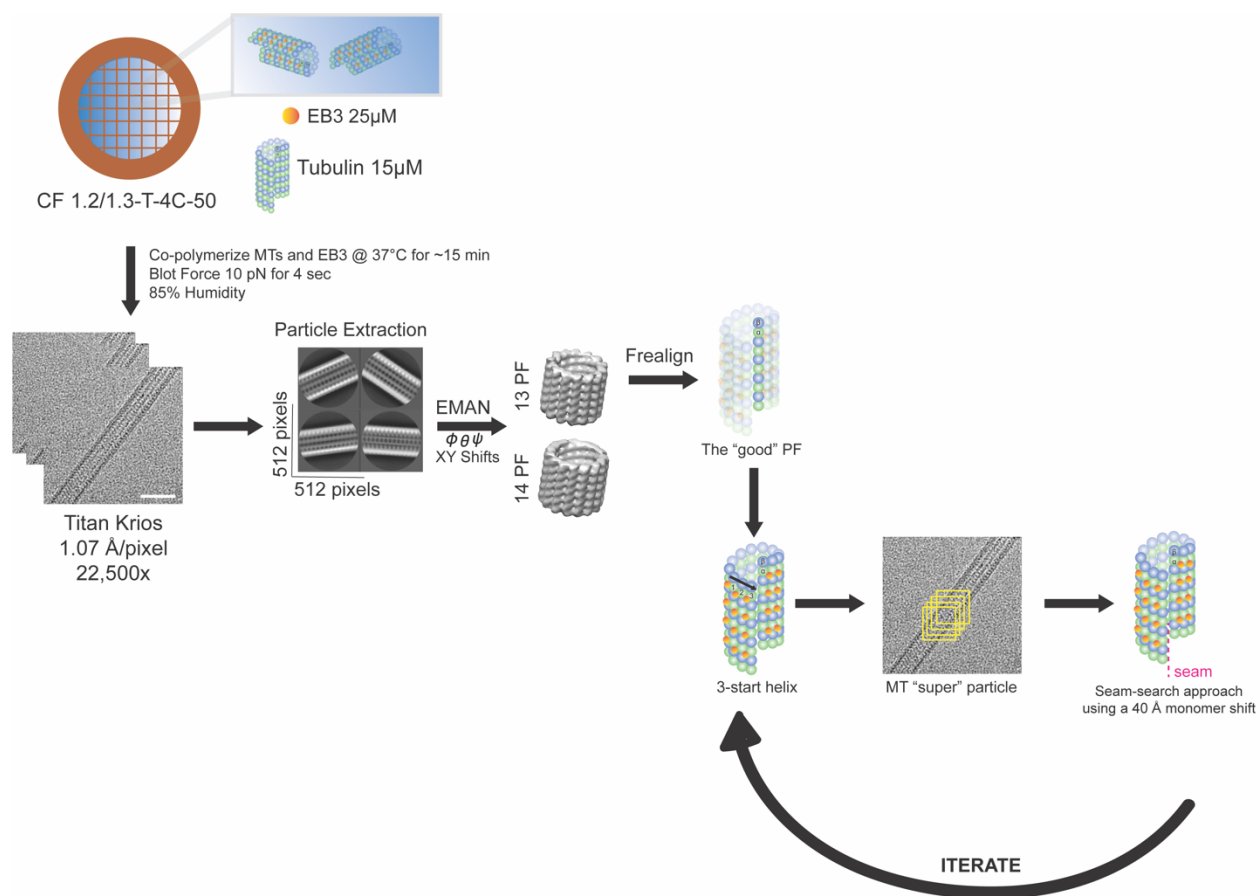
634 **Figure 4. Acetylation may weaken lateral interactions.**

635

636

637

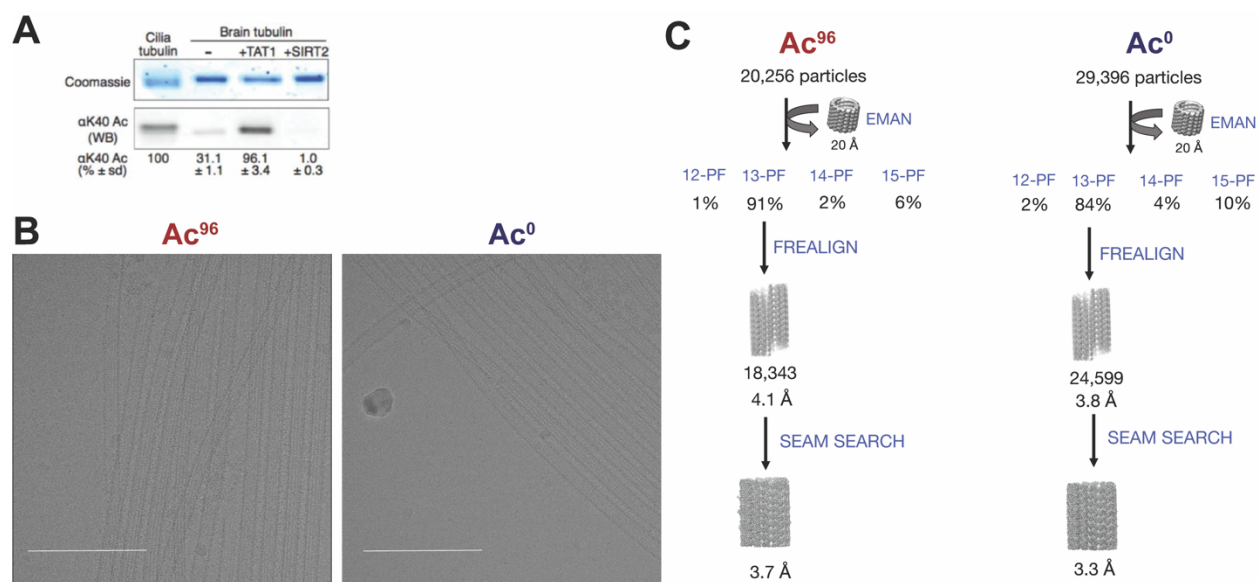




638

639 **Supplemental Figure 1. Schematic of the experimental workflow for sample**

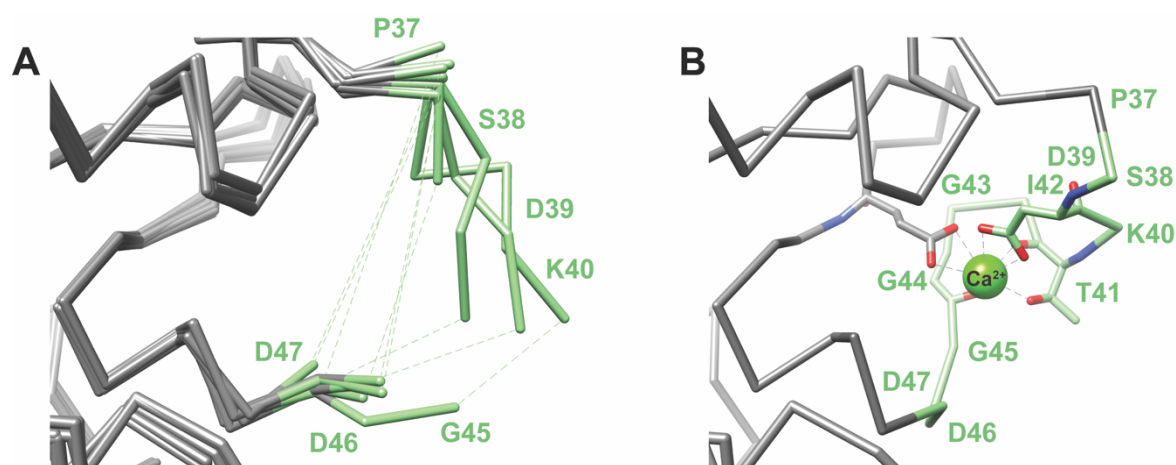
640 **preparation and pseudo-helical image processing.**



641

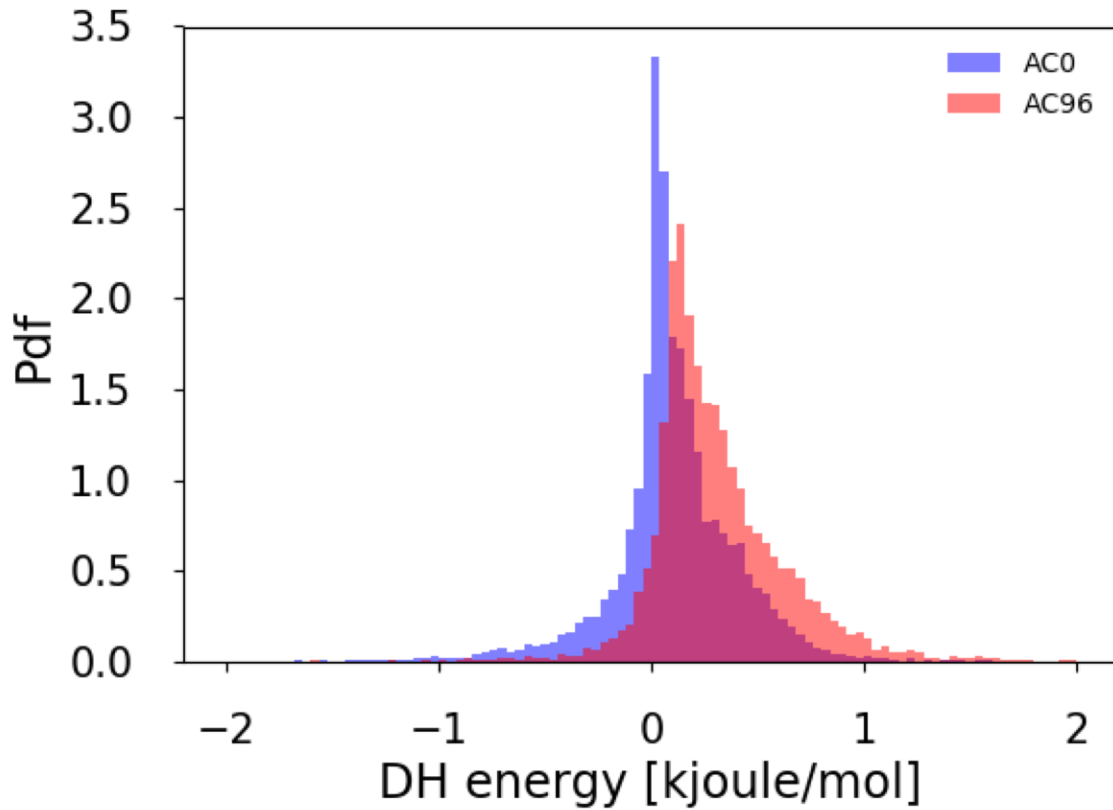
642 **Supplemental Figure 2. Sample preparation, data collection and image**

643 **processing of acetylated and deacetylated MT samples.**



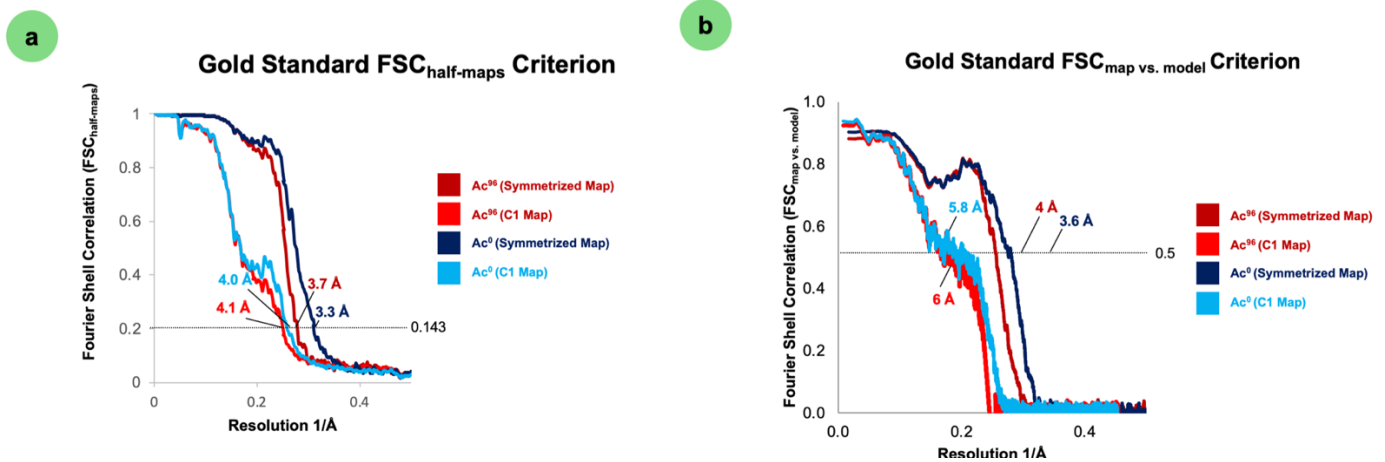
644

645 **Supplemental Figure 3. Previous proposed  $\alpha$ K40 loop models.**



646

647 **Supplemental Figure 4. Acetylation weakens lateral interactions.**



648

649 **Supplemental Figure 5. Fourier Shell Correlation Plots.**

650